

[Article]

doi: 10.3866/PKU.WHXB201310161

www.whxb.pku.edu.cn

基于不同燃料PAH特性改进的适用于多组分燃料的碳烟模型

庞 斌 解茂昭 贾 明* 刘耀东

(大连理工大学能源与动力工程学院, 海洋能源利用与节能教育部重点实验室, 辽宁 大连 116023)

摘要: 将多环芳烃(PAH)骨架模型与甲苯参比燃料(TRF)氧化模型耦合, 构建了一个新的TRF-PAH骨架模型. 以新的TRF-PAH骨架模型作为燃料燃烧的气相化学反应模型, 基于不同分子结构的燃料氧化过程中生成PAHs和碳烟的路径也不同的研究结论, 本文进一步优化了以PAHs为碳烟前驱生成物的碳烟半经验模型. 通过甲苯在流动反应器、搅拌反应器和激波管中的氧化/裂解实验验证发现, 新的TRF-PAH骨架模型可以相对准确地预测小分子PAHs和重要中间组分的浓度. 通过对比烷烃和芳香烃氧化过程中生成苯的计算值可以发现, 燃料的分子结构对PAHs的生成路径影响很大. 另外, 改进后的碳烟模型利用甲苯、正庚烷/甲苯及异辛烷/甲苯混合物为燃料的激波管中裂解和氧化实验验证, 结果表明在较宽的工况内碳烟模拟值与实验值吻合较好. 最后, 将新的碳烟模型应用于KIVA程序, 模拟以TRF20为燃料的柴油机碳烟排放, 结果表明TRF-PAH骨架模型和碳烟模型能重现缸内燃烧和排放的特性.

关键词: 甲苯参比燃料; 多环芳烃; 半经验碳烟模型; 反应机理; 直喷柴油机

中图分类号: O643

Improved Phenomenological Soot Model for Multicomponent Fuel Based on Variations in PAH Characteristics with Fuel Type

PANG Bin XIE Mao-Zhao JIA Ming* LIU Yao-Dong

(Key Laboratory of Ocean Energy Utilization and Energy Conservation of Ministry of Education,
School of Energy and Power Engineering, Dalian University of Technology, Dalian 116023, Liaoning Province, P. R. China)

Abstract: Integration of a skeletal polycyclic aromatic hydrocarbon (PAH) model with a toluene reference fuel (TRF) oxidation model was used to develop a skeletal TRF-PAH model. A phenomenological soot model, coupled with the new TRF-PAH model, was modified based on the experimental observation that fuels with different molecular structures produce PAHs and soot in different ways. The new TRF-PAH model was validated against experimental data for the relevant PAHs for the oxidation/pyrolysis of toluene in a jet-stirred reactor, flow reactor, and shock tube. The results show that the PAH model can reproduce the experimental data for the major species concentrations. The predicted benzene concentration in the oxidation of alkanes and aromatic hydrocarbons indicates that the molecular structure of the fuel significantly affects the PAH formation pathway. The improved soot model was validated against measured soot yields from the pyrolysis of toluene, toluene/*n*-heptane mixtures, and toluene/isooctane mixtures in a shock tube, as well as toluene oxidation. The results show that the predicted soot yields obtained using the new soot model are in reasonable agreement with the experimental data over a wide operating range. Finally, the soot model was used to predict the soot emissions from a diesel engine fueled with TRF20. The results indicate that the TRF-PAH combustion model and the new soot model can reproduce the combustion and emission characteristics well.

Received: July 11, 2013; Revised: October 14, 2013; Published on Web: October 16, 2013.

*Corresponding author. Email: jiaming@dlut.edu.cn; Tel: +86-411-84706302.

The project was supported by the National Natural Science Foundation of China (51176020, 51176021) and General Motors Global R&D, USA (GM024705-NV584).

国家自然科学基金(51176020, 51176021)和美国通用汽车全球研发中心(GM024705-NV584)资助项目

© Editorial office of *Acta Physico-Chimica Sinica*

Key Words: Toluene reference fuel; Polycyclic aromatic hydrocarbon; Phenomenological soot model; Chemical kinetic model; Direct-injection diesel engine

1 Introduction

As the regulation on the number and size of particulate matter (PM) from the combustion process of internal combustion (IC) engines becomes more and more stringent, it is necessary to understand the soot formation and oxidation processes. Research on the soot formation in simple reactors, such as shock tube and flow reactor, is fundamentally important for developing the models used to predict the soot emissions from IC engines.

Recently, simple fuel surrogates are generally used to represent gasoline in computational fluid dynamics (CFD) modeling for the combustion process of gasoline engine. Fuel surrogates often contain a limited number of components in order to minimize the computational time. Three practical gasoline surrogates have been extensively used for CFD modeling of the combustion of IC engines, which are *iso*-octane (C_8H_{18}), *n*-heptane (C_7H_{16}) and C_8H_{18} mixture (primary reference fuels, PRF), as well as the mixture of C_7H_{16} , C_8H_{18} , and toluene (toluene reference fuels, TRF).¹⁻³ In recent studies,³⁻⁶ ignition delay, heat release rate, and in-cylinder pressure histories are regarded as the validating parameters between the surrogate fuels and the real one. And, it is also important for the surrogate fuel to reproduce the emission characteristics as the real fuel. Particularly, the simulation of soot emission has been a long-standing challenge for researchers due to its complexities associated with fuel composition and fuel chemistry. It has been suggested that the impact of fuel molecular structure on the soot emission should be carefully considered.⁷⁻¹¹ By conducting the experiment in the counter-flow diffusion flames with three binary mixtures of C_7H_{16} , C_8H_{18} , and C_7H_8 as gasoline surrogate, Choi *et al.*⁹ found that C_7H_{16} , C_8H_{18} , and their mixtures were almost non-sooting fuel. Whereas, when C_7H_8 was added to either C_7H_{16} or C_8H_{18} , the polycyclic aromatic hydrocarbons (PAHs) and soot yield increased monotonically with increasing the C_7H_8 ratio.⁹

Several comprehensive detailed soot models have been constructed for the multi-component fuels in recent years.^{8,12,13} Agafonov *et al.*^{8,12} proposed a detailed kinetic soot model for the pyrolysis of aliphatic (methane, propane, and propylene) and aromatic (benzene, toluene, and ethyl-benzene) in a shock tube, and the detailed soot model has successfully reproduced the soot yield from those fuel. Blacha *et al.*¹³ developed a detailed soot model using a sectional approach. The model was validated against the measured data of soot for ethylene, propylene, kerosene surrogate (12% C_7H_8 , 23% C_8H_{18} , and 65% *n*-decane in volume), and C_7H_8 flames.

Although the detailed soot models are capable of accurately describing the soot and PAH formation processes for different fuels, it is too costly to use a detailed soot model in the multi-

dimensional CFD modeling of engine combustion processes. Thus, in order to improve the computational efficiency, it is necessary to develop a phenomenological soot model coupled with a skeletal PAH chemical kinetic model to predict the essential features of the fuel chemistry, as well as the formation and oxidation of PAHs and soot.

It is worth noting that, although several phenomenological soot models have been constructed to simulate the soot formation and oxidation, most of them focus only on a single fuel, such as *n*-heptane.¹⁴⁻¹⁷ Due to the large percentage of aromatics in the practical gasoline and diesel fuels, it is urgent to develop a general soot model for fuel mixtures, which can be applied to model the soot characteristics in the oxidation not only for alkane fuel, but also for other types of fuels with production of high levels of benzene (A1), such as toluene and other aromatic fuels. Thereby, the soot formation and oxidation characteristics can be accurately reproduced for the practical diesel and gasoline fuels by integrating the phenomenological soot model with the fuel surrogate model.

However, few mechanisms for the oxidation of multi-component fuels with consideration PAH sub-mechanism are available at present. Although Kaminaga *et al.*¹⁸ and Vishwanathan¹⁹ proposed a PAH model to simulate the formation of soot precursor, the PAH model has not been well validated by fundamental experiments in their studies. Wang *et al.*²⁰ developed a reduced TRF-PAH model, which was not combined with soot model. Only until recently, Zheng²¹ and Wang^{22,23} *et al.* constructed a PAH model for multi-component fuels. Whereas, the effects of fuel type on PAH and soot formations were not deeply understood yet.

The purpose of this paper is to construct a phenomenological soot model for different types of fuels (e.g., alkane and aromatic fuels) with the consideration of the PAH characteristics variation. Firstly, a skeletal TRF-PAH model was developed by coupling a TRF oxidation model with a skeletal PAH model. The new TRF-PAH model was validated against the measured data on C_7H_8 pyrolysis and oxidation in jet-stirred reactor, flow reactor, and shock tube. Then, a phenomenological soot model was modified on the basis of the TRF-PAH model in wide operating conditions. By comparing with the measured data from a shock tube for C_7H_8 , C_7H_8/C_7H_{16} mixtures, and C_7H_8/C_8H_{18} mixtures, as well as an engine fueled with TRF, the validations of the improved soot model were finally carried out.

2 Model development

2.1 Combustion chemistry model

A skeletal TRF oxidation model with 56 species and 168 reactions developed by the authors' group on the basis of the reference²⁴ was used to model the combustion chemistry in this

study. The TRF model was constructed by coupling C_7H_8 , C_7H_{16} , and C_8H_{18} oxidation sub-models based on a decoupling methodology. The TRF skeletal model has been verified with various combustion parameters including ignition delay in shock tube, propagation speed in flames, and in-cylinder pressure in internal combustion engines over wide ranges of pressure (p), equivalence ratio (ϕ), and temperature (T), on each single fuel component as well as their blends. In order to combine the TRF model with the PAH model, further improvements were made by adding necessary reactions and optimizing rates of the identified reactions, which are detailed described in the following sections.

2.2 PAH kinetic model

The skeletal PAH model was adopted from our recent study.²⁵ This model was developed by summarizing important pathways of PAHs formation with further reduction using the normalized rate of production (ROP) approach.²⁶ The typical PAHs in the model are A1, naphthalene (A2), phenanthrene (A3), and pyrene (A4). For A1 formation, the reaction $C_3H_3 + C_3H_3 = A1$ is a crucial pathway. For the large PAHs (A2, A3, and A4), the H-abstraction- C_2H_2 -addition (HACA) mechanism is used to describe the PAH growth process. Besides, the reactions, $C_3H_3 + C_3H_3 = A2$ and $A1 + A1C_2H = A3 + H$, are important pathways for large PAH formation, which are also considered in the PAH kinetic model. The PAH model has been verified with the measured data of the related PAH concentrations in C_7H_{16} and C_8H_{18} premixed laminar flames and C_7H_{16} counter-flow diffusion flames. Detailed information of the PAH model can be found in reference.²⁵

2.3 TRF-PAH model

2.3.1 Updated TRF-PAH model

The final TRF-PAH model developed in this study was built by combining the skeletal TRF oxidation model with the skeletal PAH formation model. It should be noted that the construction of the TRF-PAH model is considerably more difficult than that for alkane-PAH model due to the following three reasons. Firstly, toluene is a typical aromatic hydrocarbon whose molecular structure is completely different from that of alkane. The difference causes more complicated and diverse reaction paths for the PAH formation. Secondly, the toluene oxidation sub-model in the TRF model also affects the PAH formation processes for C_7H_{16} and C_8H_{18} . In order to accurately reproduce the PAH characteristics during the pyrolysis and oxidation of C_7H_{16} and C_8H_{18} , the calibration of the C_7H_8 oxidation sub-model should be carefully conducted. Thirdly, the PAH sub-model includes A1 formation through the polymerization of small unsaturated hydrocarbon, which was not considered in the previous TRF model. As the PAH sub-model is combined with the TRF model, it would influence the predictions of ignition delay and laminar flame speed of C_7H_8 . Therefore, a large amount of optimization work should be performed to match the measured data on the combustion characteristics of toluene, and accurately reproduce the PAH formation processes simultaneously.

In addition, 13 reactions and 4 species related to propargyl radical (C_3H_3), vinylacetylene (C_4H_4), and cyclopentadienyl radical (C_5H_5) formation were quoted from reference²⁵ to combine the TRF oxidation model with the PAH formation model. It still needs to optimize the TRF-PAH model after determining the reaction path. The detailed optimization is described as follows.

(1) The TRF-PAH model was firstly verified with the measured data on the ignition delay of C_7H_8 in wide operating conditions.^{27,28} By using sensitivity analysis, it is indicated that the reactions, $C_6H_5CH_2 + HO_2 = C_6H_5CHO + H + OH$ and $C_5H_5 + O = C_4H_5 + CO$, significantly affect the ignition delay of toluene. Thus, the rate constants of the important reactions (as listed in Table 1) were calibrated to obtain the consistent predictions as the original TRF model.

(2) By using path analysis, the individual reactions to the formation of PAHs in C_7H_8 oxidation in jet-stirred reactor were further identified. The rate of the identified reactions were modified to match the measured data of PAH concentration from jet-stirred reactor²⁹ and flow reactor³⁰ under wide experimental conditions.

(3) Step 1 and step 2 were repeated until the PAH model is able to satisfactorily reproduce both the experimental PAH concentrations^{29,30} and the ignition delay.^{27,28}

The final TRF-PAH model includes 73 species and 207 reactions. The model in CHEMKIN format can be found in the supplementary material.

2.3.2 Pathway of A1 formation for TRF

It has been found by Zhang *et al.*³¹ that A1 is made in different pathways during the oxidation of fuels with different molecular structures. However, once the A1 is produced, the subsequent pathways to large PAHs and soot are expected to be without restricting the types of fuel. According to the theoretical and experimental investigations on the PAH formation from alkane and aromatic hydrocarbons oxidation,^{2,8,9,12,13,21,31–34} the pathways of A1 formation for C_7H_{16} , C_8H_{18} , and C_7H_8 are constructed under highly sooting conditions ($T=1800$ K, $p=2.5$ MPa, $\phi=5$, and residence time (t_{res})=2 ms) in a shock tube. Fig.1 shows the schematic diagram of the final skeletal model structure, where the green solid lines represent the primary path for A1 formation. It can be seen that there is a considerable discrepancy in the pathways of A1 formation between aromatic (C_7H_8) and alkane (C_7H_{16} , C_8H_{18}). For toluene oxidation, A1 is formed rapidly due to the fact that C_7H_8 has a ring structure and produces A1 without ring-opening stages. Moreover, a large number

Table 1 Modified reactions of toluene sub-mechanism

Reaction	$A/(cm^3 \cdot mol^{-1} \cdot s^{-1})$	
	modified model	original model ²⁴
$C_6H_5CH_3 = A1 + CH_3$	8.66×10^{15}	2.66×10^{16}
$C_6H_5CH_2 + HO_2 = C_6H_5CHO + H + OH$	1.50×10^{14}	5.00×10^{14}
$C_5H_5 + O = C_4H_5 + CO$	4.20×10^{13}	3.20×10^{13}

A is the pre-exponential factor of Arrhenius formula.

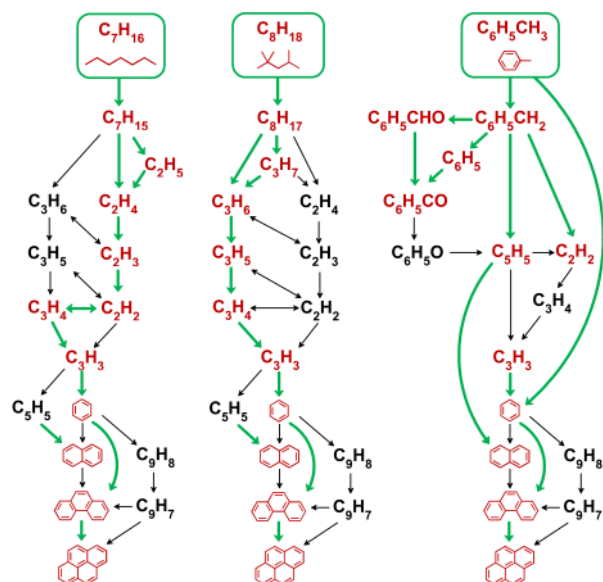


Fig.1 Schematic diagram of the skeletal model structures

of unsaturated hydrocarbons (e.g., C_2H_2 , C_3H_3 , C_4H_4 , and C_5H_5) are produced by benzyl decomposition through the reactions $C_6H_5CH_2=C_3H_5+C_2H_2$ and $C_6H_5CH_2=C_4H_4+C_3H_3$.^{35,36} Those unsaturated hydrocarbons play important roles in PAH formation and growth. However, for alkane oxidation, A1 formation process involves ring formation stages from C3 species (e.g., C_3H_3 , propyne (C_3H_4)), which results in the slower reaction rates of A1 formation.

By comparing the model structures of C_7H_{16} and C_8H_{18} shown in Fig.1, it can also be found that the combination of C_3H_3 radicals is very important for A1 formation in both C_7H_{16} and C_8H_{18} oxidation, which is consistent with recent investigations.^{31,37,38} However, it should be noted that the C_7H_{16} oxidation generates numerous C2 species (e.g., C_2H_2 , ethylene (C_2H_4)), and then yields C3 species (e.g., C_3H_3 and C_3H_4) in subsequent steps.³¹ Whereas, for the C_8H_{18} oxidation, C3 species is directly formed from the decomposition of large alkyl radicals. This results in faster reaction rates of the C3 species formation in the C_8H_{18} oxidation than that in C_7H_{16} oxidation. Moreover, C_3H_3 is primarily formed from C_3H_4 by H and OH abstraction. The reactions of C_3H_3 from C_3H_4 occurs in C_7H_{16} oxidation, but it is more important in C_8H_{18} oxidation as indicated by Marchal *et al.*³³ Therefore, more A1 is generated in C_8H_{18} flame than that in C_7H_{16} flame.

2.3.3 Sensitivity analysis of A1 formation for TRF oxidation

In order to identify the important pathways for the formation of PAHs with the variation of fuel type, the new skeletal TRF-PAH model was examined by using sensitivity analysis for C_7H_{16} , C_8H_{18} , and C_7H_8 oxidation under highly-sooting conditions ($T=1800$ K, $p=2.5$ MPa, $\phi=5$, $t_{\text{res}}=2$ ms) in a shock tube. Fig.2 shows the sensitivity coefficients related to the concentration of A1 with respect to the pre-exponential factors for three fuels at a residence time corresponding to the maximum con-

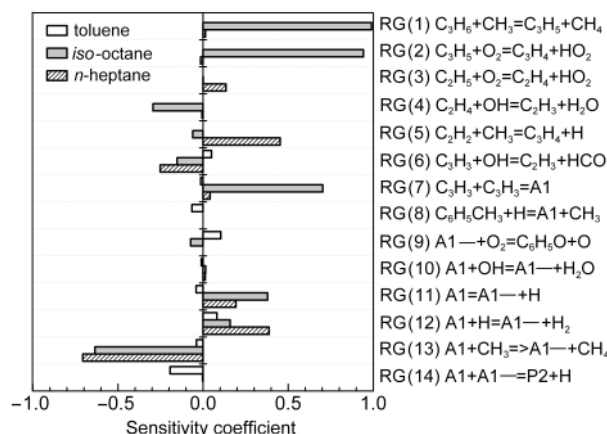


Fig.2 Sensitivity coefficient related to the concentration of A1 for C_7H_{16} , C_8H_{18} , and C_7H_8 at a residence time corresponding to maximum concentration of A1

centration of A1. As expected, the sensitive reactions for A1 formation are very different between alkane fuel and aromatic fuel. Fig.2 indicates that the dehydrogenation reactions (e.g., RG(1), RG(2), RG(3)), which increase the degree of unsaturation of the reactants with a higher reactivity, show higher sensitivity in alkane fuel than that in aromatic fuel at the residence time with maximum concentration of A1. It can also be seen that the reactions with C3 species, such as RG(1), RG(2), and RG(7), show large positive sensitivity for A1 formation in C_8H_{18} oxidation, while the reactions RG(3) and RG(5) concerned with C2 species are very important for A1 formation in C_7H_{16} oxidation, especially for the reaction RG(5) which dominates C_3H_4 production.

It is worth noting that, as a primary channel for A1 formation, RG(8) shows negative sensitivity for A1 in C_7H_8 oxidation. This is primarily due to the fact that the high level of A1 concentration at the end of C_7H_8 oxidation leads to an increased reverse reaction rate of RG(8).

2.4 Phenomenological soot model

The soot model used in the present study is based on our previously developed soot model²⁵ for C_7H_{16} combustion. The soot formation and oxidation processes are simplified into six processes such as soot precursor formation *via* conversion of precursor species (C_2H_2 , A3, and A4), soot inception, soot growth by C_2H_2 and A1 surface deposition, soot coagulation, soot oxidation *via* OH and oxygen (O_2), and soot precursor oxidation. More about the basic soot model has been described in reference.²⁵ It should be noted that the previous soot model was developed primarily focusing on modelling of soot emissions for C_7H_{16} oxidation.²⁵ Based on the fact that the PAH and soot formation characteristics vary with different fuel molecular structures, the pre-exponential factors of soot inception and surface growth reactions were improved in this study in order to extend the soot model for the simulation of the pyrolysis and oxidation of C_7H_{16} , C_8H_{18} , and C_7H_8 . Moreover, the OH-related soot oxidation model is introduced from the work of Fenimore and Jones³⁹ instead of the previous model by Neoh *et al.*⁴⁰ This

Table 2 Modified reactions of soot model

Reaction	Modified model	Original model ²³
$C_2H_2 \rightarrow 0.04C(PR)_{50} + H_2$	$k'_1 = k_1$	$k_1 = 4.00 \times 10^5 T^0 \exp(-1.6383 \times 10^5/RT)$
$A3 \rightarrow 0.28C(PR)_{50} + 5H_2$	$k'_2 = 2.00 \times 10^8 T^0 \exp(-1.6383 \times 10^5/RT)$	$k_2 = 1.0 \times 10^6 T^0 \exp(-1.6383 \times 10^5/RT)$
$A4 \rightarrow 0.32C(PR)_{50} + 5H_2$	$k'_3 = 2.00 \times 10^8 T^0 \exp(-1.6383 \times 10^5/RT)$	$k_3 = 5.0 \times 10^9 T^0 \exp(-1.6383 \times 10^5/RT)$
$C(PR)_{50} \rightarrow 0.5C(S)_{100}$	$k'_4 = k_4$	$k_4 = 4.1 \times 10^{11} T^0 \exp(-3.7436 \times 10^4/RT)$
$C(S)_m + C_2H_2 \rightarrow C(S)_{m+2} + H_2$	$k'_5 = k_5$	$k_5 = 4.05 \times 10^3 T^0 \exp(-2.5789 \times 10^4/RT)$
$C(S)_m + A1 \rightarrow C(S)_{m+6} + 3H_2$	$k'_6 = 4.03 \times 10^4 T^0 \exp(-2.5789 \times 10^4/RT)$	$k_6 = 1.03 \times 10^4 T^0 \exp(-2.5789 \times 10^4/RT)$
$nC(S)_m \rightarrow C(S)_{n+m}$	Kazakov-Foster model	Kazakov-Foster model
$C(PR)_{50} + 25O_2 \rightarrow 50CO$	$k'_7 = 1.00 \times 10^9 T^0 \exp(-1.6383 \times 10^5/RT)$	$k_7 = 1.00 \times 10^9 T^0 \exp(-1.6383 \times 10^5/RT)$
$C(S)_m + O_2 \rightarrow C(S)_{m+2} + 2CO$	NSC model	NSC model
$C(S)_m + 2OH \rightarrow C(S)_{m+2} + 2CO + H_2$	increased Fenimore and Jones rate ³⁹ by a factor of 4.7	Neoh <i>et al.</i> model ⁴⁰

PR: precursor. $k = AT^0 \exp(-E/RT)$. unit: A , $cm^3 \cdot mol^{-1} \cdot s^{-1}$; E , $J \cdot mol^{-1}$

is due to the fact that the OH-related oxidation model from Neoh *et al.*⁴⁰ predicts higher soot oxidation rate than the measurements in the conventional diesel combustion conditions, which is also found by Vishwanathan.¹⁹ The modified reactions of the soot model are summarized in Table 2. By optimizing these reaction rates, the measured soot yield could be accurately reproduced by the improved soot model for the pyrolysis and oxidation of C_7H_{16} ,⁴¹ C_7H_8 ,⁴² C_7H_8/C_7H_{16} mixtures and C_7H_8/C_8H_{18} mixtures⁷ in shock tube.

3 Validation of the TRF-PAH model

The validations presented in this section for flow reactor, jet-stirred reactor, and shock tube were simulated by CHEMKIN PRO with a zero-dimensional gas-phase kinetics model. Since the combustion characteristics (e.g., ignition delay and laminar flame speed) of the new TRF-PAH model were consistent with those of the previous TRF model,²⁴ the corresponding predictions were shown in this study.

3.1 Validations of toluene oxidation in flow reactor

Klotz *et al.*²⁹ carried out an experiment about the oxidation of C_7H_8 in an atmospheric-pressure flow reactor at a high temperature (1173 K) by means of gas chromatographic analysis. Comparisons between the simulated and the experimental data on the concentration profiles of C_7H_8 and carbon monoxide (CO) are shown in Fig.3. The simulation results from the original TRF model without PAH model, semi-detailed mechanism 1 (Sakai *et al.*⁴³) and semi-detailed mechanism 2 (Andrae *et al.*⁴⁴) are also illustrated for comparison. Fig.3 indicates that the concentration profiles of the reactants (e.g., C_7H_8) and the products (e.g., CO) are well reproduced by the new skeletal TRF-PAH model. The overall predictions from the new model are better than those by the other three mechanisms, especially during the later stages of C_7H_8 decay. It is probably because the updated pathways of A1 formation lead to relatively slower reaction rates for the C_7H_8 decomposition. Two of the improved reactions are $A1 = A1 + H$, which shows a large positive sensitivity for A1 formation, and $C_6H_5CH_2 + HO_2 = C_6H_5CHO + H + OH$, which shows a large negative sensitivity for A1 formation as discussed in Section 2.3.3.

Furthermore, the main attention is focused on the validation of C_2H_2 and A1 evolutions, because C_2H_2 plays an important role for large PAH formation and soot surface growth, and A1 is a potential precursor for large PAHs. The experimental and simulated concentration profiles for four major species are plotted in Fig.4. The results show that the predicted results from the new TRF-PAH model are in good agreement with the measured data. Moreover, the higher concentration of A1 than that of C_2H_2 in the C_7H_8 oxidation process is also well reproduced by the model. This trend is opposite during the C_7H_{16} or C_8H_{18} oxidation processes, which produce much higher levels of C_2H_2 than those of A1.^{25,45} Thus, in previous soot models with only C_2H_2 as soot precursor species, the soot formation with the variation of fuel type cannot be well predicted. It is one of the reasons for using PAHs as soot precursor species in the improved soot model.

3.2 Validations of toluene oxidation in jet-stirred reactor

The experiments for toluene oxidation in a jet-stirred reactor were carried out by Dagaut *et al.*³⁰ at the pressure of 1.0 MPa and equivalence ratio of 1.5 over a temperature range from 1000 to 1375 K for a residence time of 1.2 ms. The concentrations of stable species were measured by gas chromatographs with the uncertainties in the range of 5%–10%. Fig.5 shows mole fractions of major species as a function of initial temperature. The simulations were conducted with the new skeletal model and the original TRF model for comparison. From Fig.5, it can be seen that trends and magnitude of the predicted mole fraction from new TRF-PAH model are both in good agreement with the experimental values of the reactants (e.g., C_7H_8 and O_2), products (e.g., H_2O and CO), and soot precursor species (e.g., C_2H_2 and A1). The predictions from the new model are much better than those by using the original model, especially at high temperatures. The reason for this improvement is similar with that for the inhibition of C_7H_8 decay in flow reactor as discussed in Section 3.1.

3.3 Validations of toluene pyrolysis in shock tube

The PAH formation during the C_7H_8 pyrolysis, was experimentally investigated by Colket *et al.*³² in a shock tube over

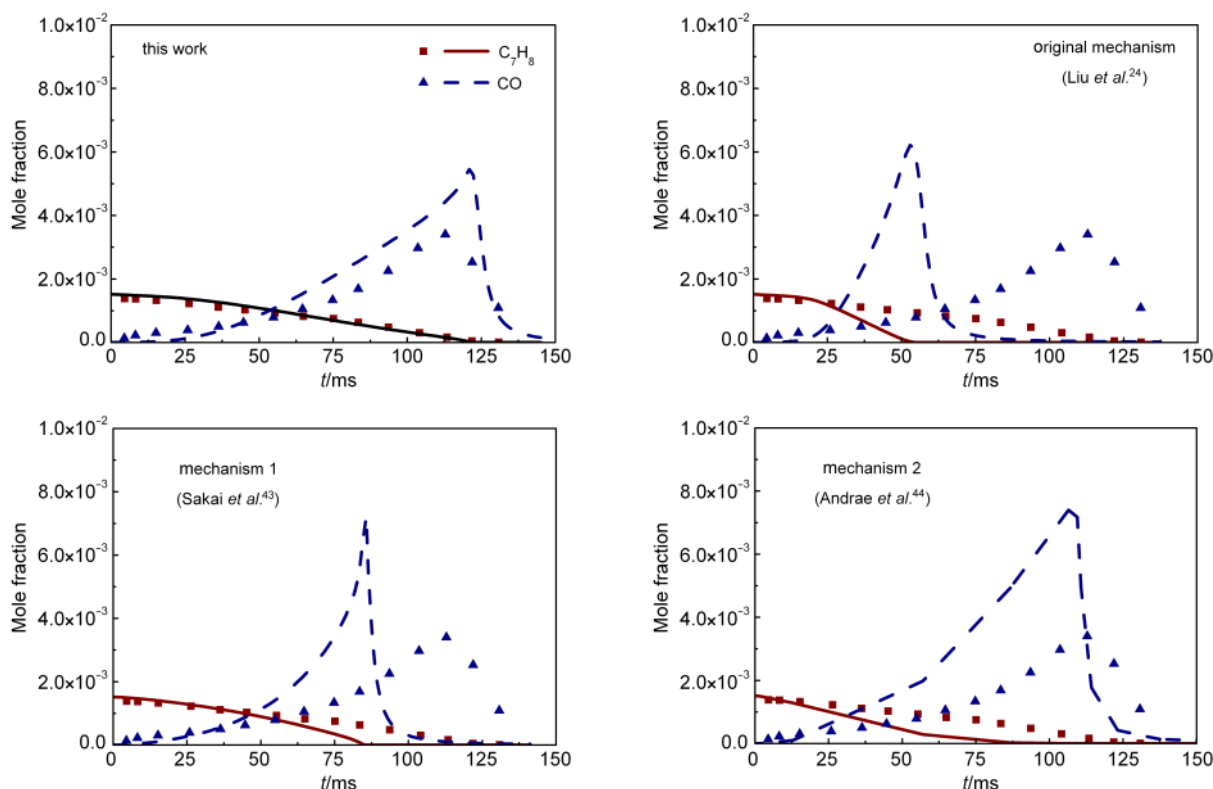


Fig.3 Comparisons between the experimental data (symbols)²⁹ and simulated results (lines) of C_7H_8 and CO concentrations in flow reactor for C_7H_8 oxidation

$T=1173\text{ K}$, $p=0.1\text{ MPa}$

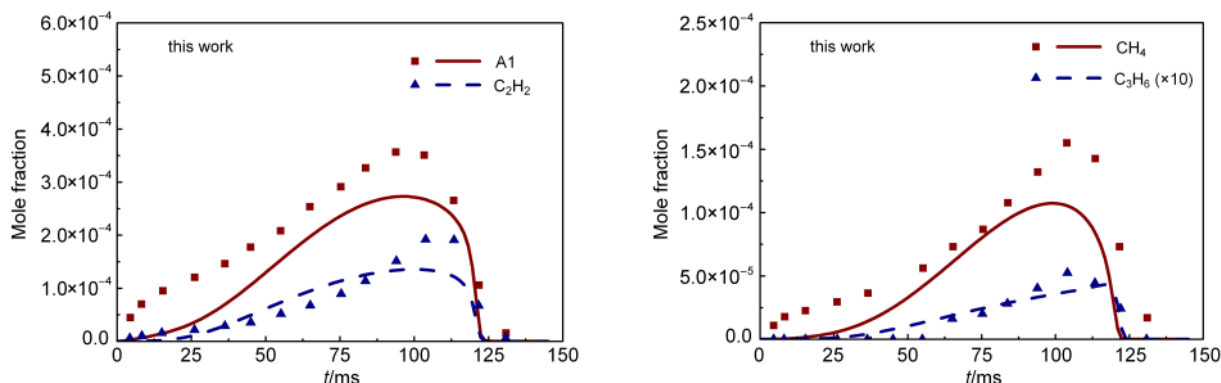


Fig.4 Comparisons between the experimental data (symbols)²⁹ and simulated results (lines) of major species concentrations in flow reactor for C_7H_8 oxidation

$T=1173\text{ K}$, $p=0.1\text{ MPa}$

temperatures ranged from 1200 to 1850 K for 1% C_7H_8 in Ar at 1.013 MPa for residence time near 600 μs . The gas sample was analyzed by a mass selective detector. Comparisons between the experimental and simulated results for the concentrations of C_7H_8 , CH_4 , and PAHs (e.g., A1, A2) at 600 μs after the reflected shock arrival are shown in Fig.6. The simulations were conducted with both the new TRF-PAH model and the detailed mechanism from Raj *et al.*³⁴ This results indicate that both the mechanisms have the ability to well reproduce the experimental data. Moreover, at high temperatures, the predicted toluene concentration by the skeletal model shows better agreement

with the measured data, whereas the detailed mechanism shows excessive C_7H_8 depletion. However, the mole fraction of A2 was underestimated by the new skeletal model since the deficient C5 sub-model produces more C_5H_5 radical, which is the major species for A2 formation by the reaction $2C_5H_5=A2+2H$ in toluene pyrolysis. Thus, further improvement of the C5 sub-model is still necessary in our next work.

4 Validations for soot model

4.1 Validation of soot yield in shock tube

In this section, the newly improved soot model was applied

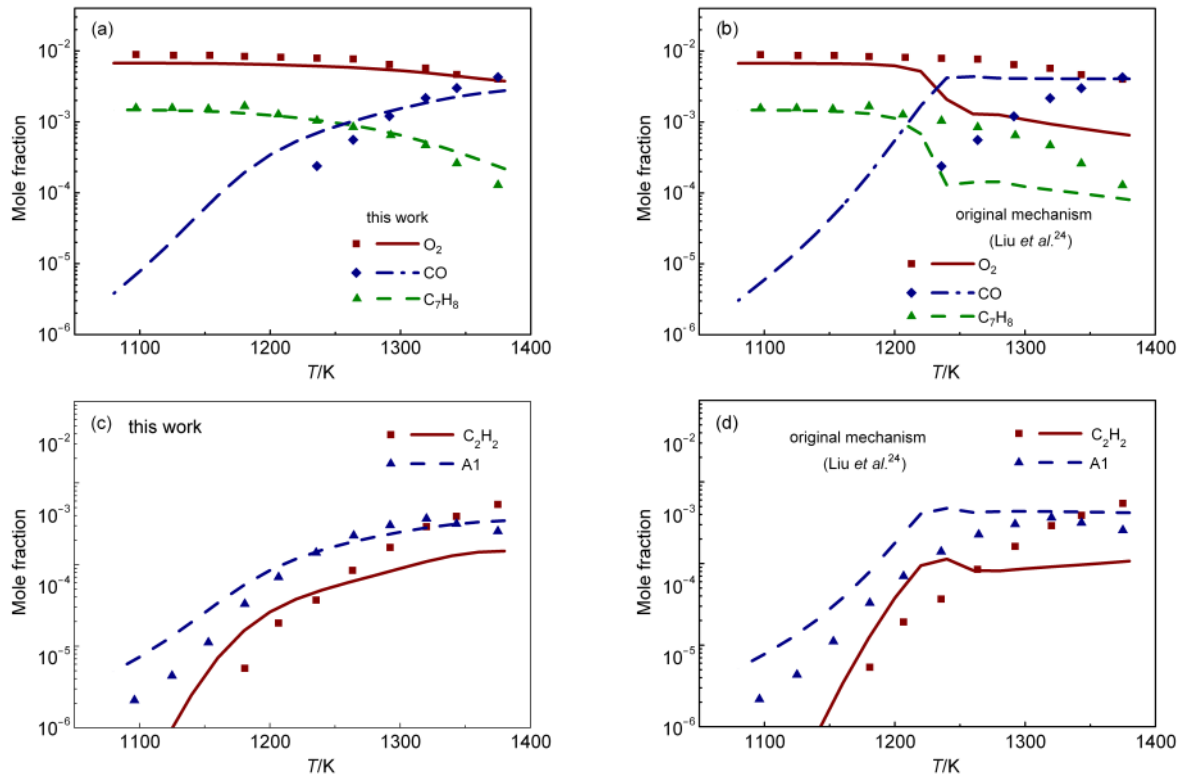


Fig.5 Comparisons between the experimental data (symbols)³⁰ and simulated results (lines) of major species concentrations in jet-stirred reactor for C_7H_8 oxidation

$p=1.0$ MPa, $\phi=1.5$, $t_{res}=1.2$ ms; (a, b) mole fractions of O_2 , C_7H_8 , and CO ; (c, d) mole fractions of C_2H_2 and $A1$

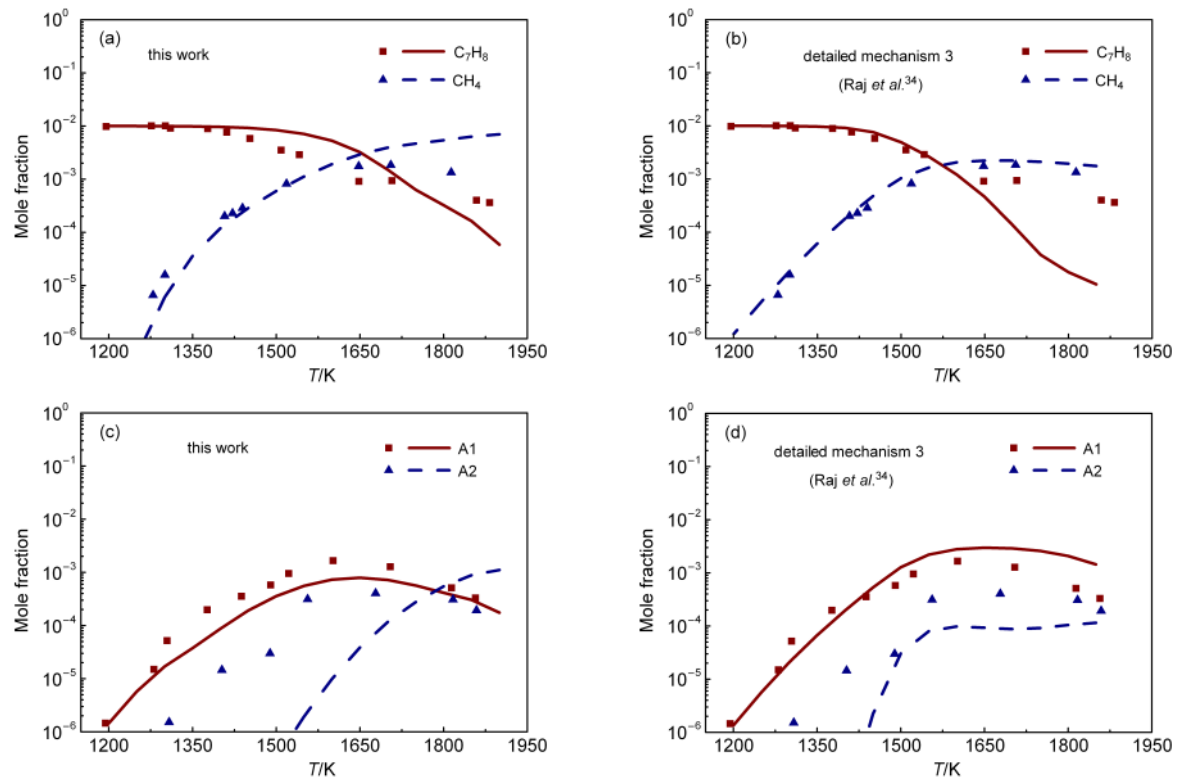


Fig.6 Comparisons between the experimental data (symbols)³² and simulated results (lines) of major species concentrations in shock tube for C_7H_8 pyrolysis

$p=1.013$ MPa; (a, b) mole fractions of C_7H_8 and CH_4 ; (c, d) mole fractions of $A1$ and $A2$

to simulate the experimental measurements performed by Alexiou and Williams for soot yield in the C_7H_8 /Ar pyrolysis, the C_7H_8 oxidation,⁴² and the TRF pyrolysis⁷ behind reflected shock waves. All the simulations were carried out by a constant-volume homogeneous adiabatic gas-phase kinetics model.

4.1.1 Validation of soot yield for toluene pyrolysis and oxidation

The comparisons results between the simulations and experiments for soot yield profiles as a function of initial temperature in the pyrolysis of various C_7H_8 /Ar mixtures are shown in Fig. 7 (a, b). The results indicate that the predicted profiles are in reasonable agreement with the experimental data, where the soot yield reaches the peak and then decreases with the increase in temperature, showing a bell-shaped distribution. The soot yield also increases with an increase in the toluene ratio in C_7H_8 /Ar mixtures, which is well reproduced by the model, as shown in Fig. 7(a, b). The sensitivity analysis reveals that C_2H_2 is mainly formed through the reaction $C_6H_5CH_2=C_5H_5+C_2H_2$, especially at high temperatures, which further accelerates the soot particle growth by C_2H_2 deposition. Thus, the rate constants of the reaction were improved in this study in order to accurately reproduce the soot yield in the range of high temperatures (2000–2400 K). Overall, the predictions exhibit reasonable agreements with the measured data for the peak value and the evolution tendency of soot yield with temperature, although there are some discrepancies between the predictions and the mea-

surements for the cases with low C_7H_8 concentration.

The comparison between the predicted and measured soot yields during the C_7H_8 pyrolysis and oxidation processes is shown in Fig. 7(c, d). For the peak value and the evolution tendency with temperature, the soot model well reproduces the soot yield at low temperatures, but slightly over-predicts the soot yield at high temperatures. Fig. 7(c, d) shows that the increase in initial oxygen concentration not only decreases the peak soot yield but also shifts the region with high soot yield to lower temperatures, which is consistent with the measurements. This is mainly due to the strong oxidation by OH and O_2 at high temperatures as oxygen is introduced. Moreover, The study of Frenklach *et al.*⁴⁶ indicated that the initial attack of the O_2 molecular on C_7H_8 causes the rapid rates reactions for unsaturated hydrocarbons (e.g., C_2H_2 , C_4H_4) and C_6H_6 formation at lower temperatures, which subsequently alters the ease of soot formation. Therefore, the peak of soot yield moves toward lower temperatures with the O_2 addition. The chain reaction of O_2 with H is more important at higher temperatures, and produces a large amount of O and OH, which enhances the soot oxidation by OH. However, the increase in the H concentration also contributes to the shift of the region with high soot yield to lower temperatures, because higher H concentration not only accelerates the combustion rate but also increases the PAH and soot formation rate.⁴⁷ Unfortunately, the soot model over-rated the soot yield under higher temperatures.

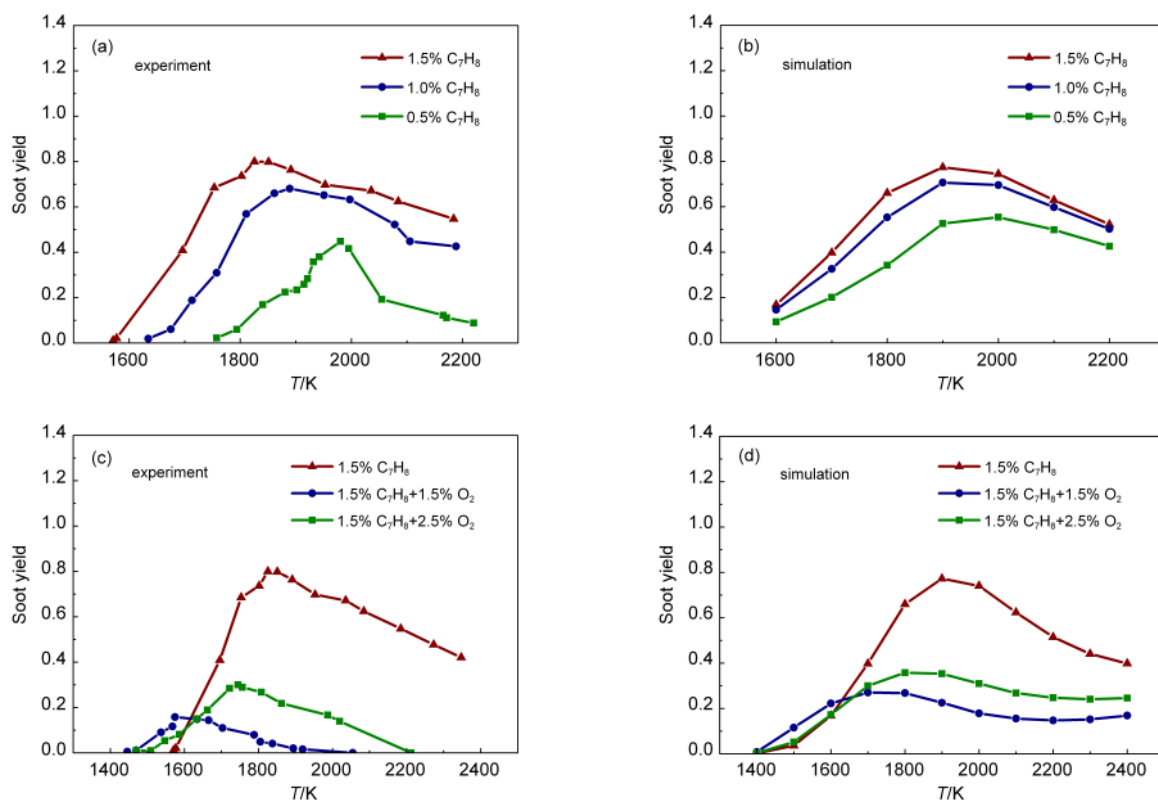


Fig. 7 Experimental⁴² and simulated soot yield as the function of temperature in shock tube

(a, b) C_7H_8 pyrolysis at $t_{res}=2$ ms; (\blacktriangle) $p=0.35$ MPa, (\blacksquare) $p=0.33$ MPa, (\bullet) $p=0.25$ MPa;

(c, d) C_7H_8 oxidation at $t_{res}=2$ ms; (\blacktriangle) $p=0.35$ MPa, (\blacksquare) $p=0.20$ MPa, (\bullet) $p=0.20$ MPa

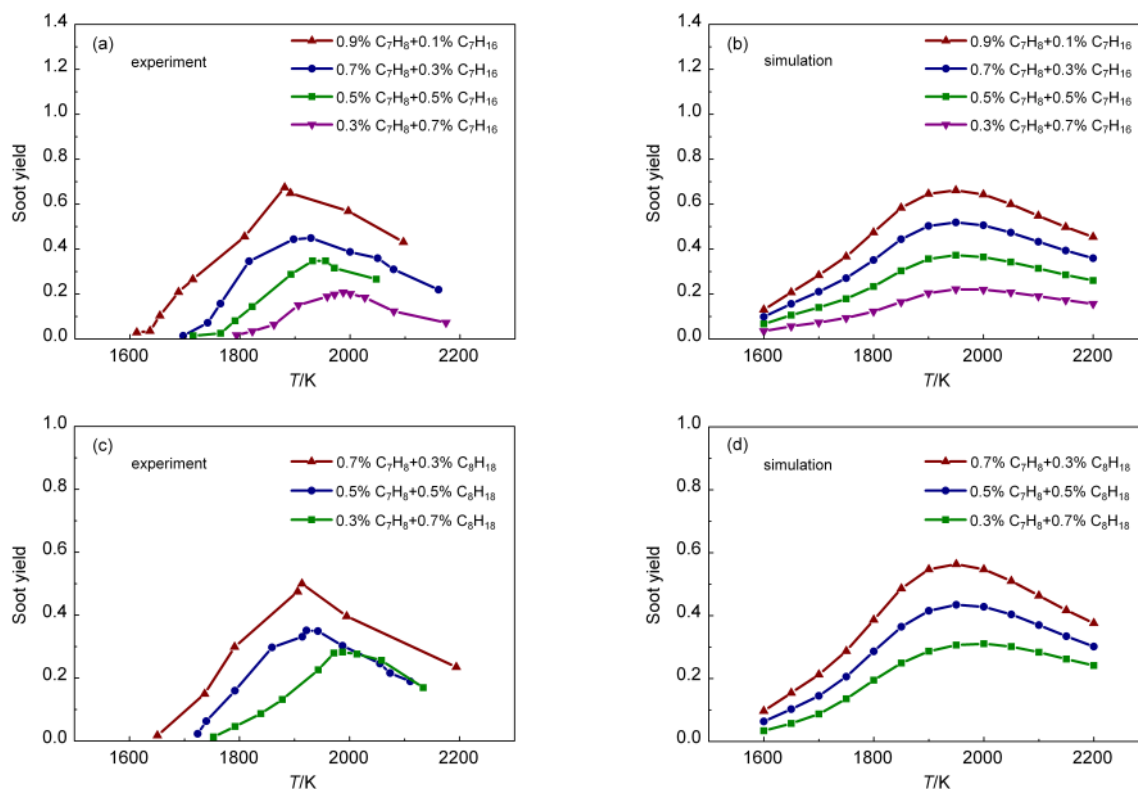


Fig.8 Experimental⁷ and simulated soot yield as the function of temperature in shock tube
(a, b) C_7H_8/C_7H_{16} mixtures pyrolysis at $t_{\text{res}}=2$ ms, $p=0.3$ MPa; (c, d) C_7H_8/C_8H_{18} mixtures pyrolysis at $t_{\text{res}}=2$ ms, $p=0.3$ MPa

4.1.2 Validation of soot yield for TRF pyrolysis

Fig.8(a, b) demonstrates the modeled soot yield from the C_7H_{16}/C_7H_8 mixtures pyrolysis at $t_{\text{res}}=2$ ms. As shown, reasonable agreement between the simulations and experiments is achieved. It is noteworthy that the soot yield is reduced with the increased C_7H_{16} fraction in the fuel mixture. The reason is that a larger amount of PAHs are produced in C_7H_8 pyrolysis than in alkane pyrolysis, which results in faster reaction rates of soot formation and surface growth reactions. So, the soot yield cannot be well reproduced by those soot models using C_2H_2 as the only soot precursor species without considering the PAH effect.

The similar results for soot yield are obtained when C_8H_{18} is used to substitute C_7H_{16} for the pyrolysis of C_7H_8/C_7H_{16} mixtures, as shown in Fig.8(c, d). By comparing Fig.8(a, b) (0.3% $C_7H_8+0.7\%$ C_7H_{16}) with Fig.8(c, d) (0.3% $C_7H_8+0.7\%$ C_8H_{18}), a large discrepancy can be found in the maximum soot yield between C_7H_8/C_7H_{16} mixture and C_7H_8/C_8H_{18} mixture: 37.2% for C_7H_8/C_7H_{16} mixture and 43.4% for C_7H_8/C_8H_{18} mixture. This is because the formation of A1 and PAHs rapidly occurs in the C_8H_{18} pyrolysis. More detailed discussion about the pathways of A1 formation in C_7H_{16} and C_8H_{18} oxidation can be found in reference.²⁵ Therefore, more soot is formed in C_7H_8/C_8H_{18} mixture than in C_7H_8/C_7H_{16} mixture at the same mixing ratio.

4.2 Validation of soot emissions in an engine fueled with TRF

In this section, the soot emissions in a direct injection (DI)

diesel engine fueled with TRF20 (80% $C_7H_{16}+20\%$ C_7H_8 in volume ratio) were simulated by the improved soot model. The experimental research about the combustion and emission characteristics of TRF20 in the diesel engine for different intake oxygen ratio ($[O_2]_{\text{in}}$) ranging from 21% to 11% at $1400 \text{ r} \cdot \text{min}^{-1}$ engine speed was investigated by Lou *et al.*⁴⁸ The tested engine is a single-cylinder diesel engine with a compression ratio of 16 and bore \times stroke of 105 mm \times 125 mm. The KIVA-3V code with several improved physical and chemistry sub-models is used to perform the simulations. More details about the computational model can be found in reference.²⁵ In order to reduce the computational time, a 45° sector of the computational mesh as shown in Fig.9 was used in this study. Fig.10 indicates that the predicted heat release rate and pressure under different intake O_2 ratio well match the measured data.

The comparison between the predictions and measurements for the soot emissions under different intake O_2 ratios is demonstrated in Fig.11. It can be seen that the overall trend of soot emission as a function of intake O_2 ratio is well reproduced by the model. Both model and experiment indicate that the soot emission reaches the peak at 12.5% intake O_2 ratio. For higher intake O_2 ratio, almost no soot emission is formed since the fuel is completely oxidized and small quantities of soot precursor species (e.g., C_2H_2 and PAHs) are produced. For the case with the intake O_2 ratio of 11%, such a quite low oxygen concentration leads to a very low combustion temperature inhibiting the soot formation, which is also reproduced by the model

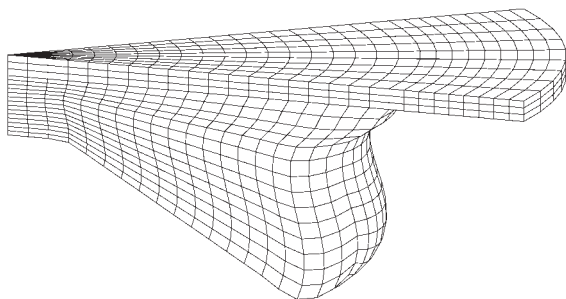


Fig.9 Computational mesh for the simulation of a DI engine

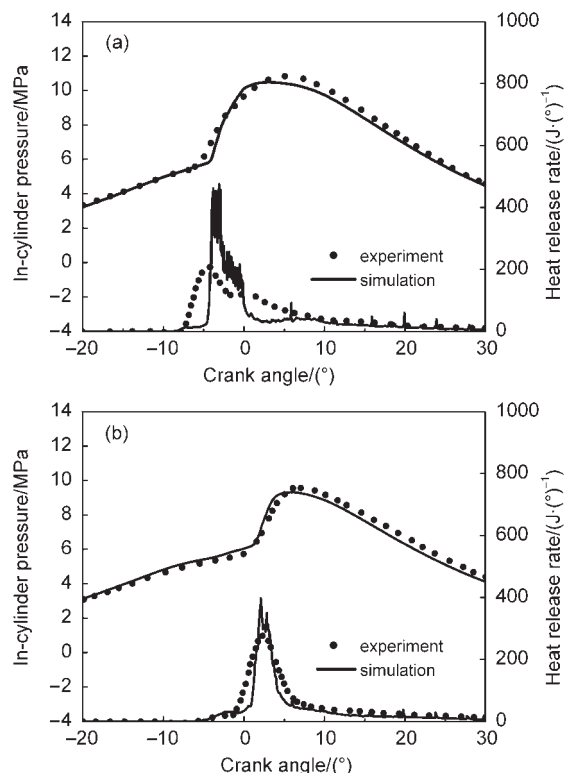


Fig.10 Comparison of the heat release rate and pressure between experimental and simulated⁴⁸ results under different intake O_2 ratio

(a) $[O_2]_{in}=18\%$; (b) $[O_2]_{in}=12.5\%$

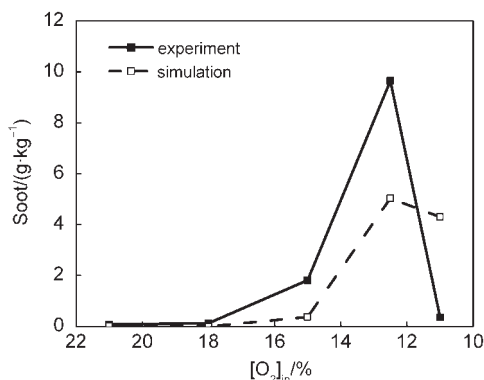


Fig.11 Comparison of soot emission between experimental and simulated⁴⁸ results under different intake O_2 ratio

reasonably well. However, there still exist some discrepancies between the predictions and measurements, such as the over-

prediction of heat release rate at 18% intake O_2 ratio and the over-estimation of soot emissions at 11% intake O_2 ratio. Thus, further improvement of the oxidation mechanism and soot model, as well as computational model still should be performed in the next work if more experimental data are available.

5 Conclusions

In the present work, a new skeletal TRF-PAH model was developed on the basis of the experimental observation that different molecular structures of fuel make soot in different ways. The new TRF-PAH model was validated against the measured data on the related PAHs concentrations for C_7H_8 oxidation/pyrolysis in flow reactor, jet-stirred reactor, and shock tube. The results indicate that the new skeletal TRF-PAH model is able to well predict the concentrations of PAHs and other major species, and is more superior to the basic TRF model without the PAH sub-model.

An optimized phenomenological soot model was coupled with the new skeletal TRF-PAH model and validated by comparing the predicted soot yield with the experimental measurements for the oxidation/pyrolysis of C_7H_8 , C_7H_8/C_7H_{16} mixtures, and C_7H_8/C_8H_{18} mixtures in a shock tube. The results demonstrate that the soot model provides reasonably quantitative predictions for soot yield with the dependences on fuel type and temperature. Due to the compact size of the skeletal TRF-PAH model, it can be easily integrated into multidimensional CFD simulation for engine combustion processes. Therefore, the soot model was finally applied to predict the in-cylinder pressures and soot emissions of a DI diesel engine fueled with TRF20 under different intake O_2 ratio conditions. It is found that the trend of soot emission as a function of intake O_2 ratio is reproduced by the model reasonably well.

Supporting Information: available free of charge via the internet at <http://www.whxb.pku.edu.cn>.

References

- (1) Ra, Y.; Reitz, R. D. *Combust. Flame* **2008**, *155* (4), 713. doi: 10.1016/j.combustflame.2008.05.002
- (2) Ra, Y.; Reitz, R. D. *Combust. Flame* **2011**, *158* (1), 69. doi: 10.1016/j.combustflame.2010.07.019
- (3) Andrae, J. C.; Björnbohm, P.; Cracknell, R.; Kalghatgi, G. *Combust. Flame* **2007**, *149* (1), 2.
- (4) Mehl, M.; Pitz, W. J.; Westbrook, C. K.; Curran, H. J. *Proc. Combust. Inst.* **2011**, *33* (1), 193.
- (5) Machrafi, H.; Cavadias, S. *Combust. Flame* **2008**, *155* (4), 557. doi: 10.1016/j.combustflame.2008.04.022
- (6) Zheng, D.; Zhong, B. J. *Acta Phys. -Chim. Sin.* **2012**, *28* (9), 2029. [郑东, 钟北京. 物理化学学报, **2012**, *28* (9), 2029.] doi: 10.3866/PKU.WHXB201207042
- (7) Alexiou, A.; Williams, A. *Fuel* **1995**, *74* (2), 153. doi: 10.1016/

- 0016-2361(95)92648-P
- (8) Agafonov, G.; Naydenova, I.; Vlasov, P.; Warnatz, J. *Proc. Combust. Inst.* **2007**, *31* (1), 575. doi: 10.1016/j.proci.2006.07.191
- (9) Choi, B. C.; Choi, S. K.; Chung, S. H. *Proc. Combust. Inst.* **2011**, *33* (1), 609. doi: 10.1016/j.proci.2010.06.067
- (10) Song, J. O.; Song, C. L.; Tao, Y.; Lv, G.; Dong, S. R. *Combust. Flame* **2011**, *158* (3), 446. doi: 10.1016/j.combustflame.2010.09.017
- (11) Chen, W. M.; Shuai, S. J.; Wang, J. X. *Fuel* **2009**, *88* (10), 1927. doi: 10.1016/j.fuel.2009.03.039
- (12) Agafonov, G.; Smirnov, V.; Vlasov, P. *Proc. Combust. Inst.* **2011**, *33* (1), 625. doi: 10.1016/j.proci.2010.07.089
- (13) Blacha, T.; Di Domenico, M.; Gerlinger, P.; Aigner, M. *Combust. Flame* **2012**, *159* (1), 181. doi: 10.1016/j.combustflame.2011.07.006
- (14) Tao, F.; Golovitch, V. I.; Chomiak, J. *Combust. Flame* **2004**, *136* (3), 270. doi: 10.1016/j.combustflame.2003.11.001
- (15) Tao, F.; Foster, D. E.; Reitz, R. D. SAE Tech. Pap. Ser. 2006, 2006-01-0196.
- (16) Vishwanathan, G.; Reitz, R. D. SAE Tech. Pap. Ser. 2008, 2008-01-1331.
- (17) Jia, M.; Peng, Z. J.; Xie, M. Z. *Proc. Inst. Mech. Eng. Part: D J. Automob. Eng.* **2009**, *223* (3), 395. doi: 10.1243/09544070JAUTO993
- (18) Kaminaga, T.; Kusaka, J.; Ishii, Y. *Int. J. Engine. Res.* **2008**, *9* (4), 283. doi: 10.1243/14680874JER00908
- (19) Vishwanathan, G. Development and Application of a Practical Soot Modeling Approach for Low Temperature Diesel Combustion. Ph. D. Dissertation, The University of Wisconsin: Madison, 2012.
- (20) Wang, F.; Zheng, Z.; He, Z. *Energy & Fuels* **2012**, *26* (3), 1612. doi: 10.1021/ef201937k
- (21) Zheng, D.; Zhang, Y. P.; Zhong, B. J. *Acta Phys. -Chim. Sin.* **2013**, *29* (6), 1154. [郑东, 张云鹏, 钟北京. 物理化学学报, **2013**, *29* (6), 1154.] doi: 10.3866/PKU.WHXB201303201
- (22) Wang, H.; Reitz, R. D.; Yao, M.; Yang, B.; Jiao, Q.; Qiu, L. *Combust. Flame* **2012**, *163* (3), 504.
- (23) Reitz, R. D.; Wang, H.; Jiao, Q.; Yao, M.; Yang, B.; Qiu, L. *Int. J. Engine. Res.* **2013**, *14* (5), 434. doi: 10.1177/1468087412471056
- (24) Liu, Y. D.; Jia, M.; Xie, M. Z.; Pang, B. *Energy & Fuels* **2013**, *27* (8), 4899. doi: 10.1021/ef4009955
- (25) Pang, B.; Xie, M. Z.; Jia, M.; Liu, Y. D. *Energy Fuels* **2013**, *27* (3), 1699. doi: 10.1021/ef400033f
- (26) Pang, K. M.; Ng, H. K.; Gan, S. *Fuel* **2011**, *90* (9), 2902. doi: 10.1016/j.fuel.2011.04.027
- (27) Shen, H. P. S.; Vanderover, J.; Oehlschlaeger, M. A. *Proc. Combust. Inst.* **2009**, *32* (1), 165. doi: 10.1016/j.proci.2008.05.004
- (28) Davis, S.; Wang, H.; Breinsky, K.; Law, C. *Symposium (International) on Combustion* **1996**, *26* (1), 1025.
- (29) Klotz, S. D.; Brezinsky, K.; Glassman, I. *Symposium (International) on Combustion* **1998**, *27* (1), 337.
- (30) Dagaut, P.; Pengloan, G.; Ristori, A. *Phys. Chem. Chem. Phys.* **2002**, *4* (10), 1846. doi: 10.1039/b110282f
- (31) Zhang, H. R.; Eddings, E. G.; Sarofim, A. F.; Westbrook, C. K. *Proc. Combust. Inst.* **2009**, *32* (1), 377. doi: 10.1016/j.proci.2008.06.011
- (32) Colket, M.; Seery, D. *Symposium (International) on Combustion* **1994**, *25* (1), 883.
- (33) Marchal, C.; Delfau, J.; Vovelle, C.; Moreac, G.; Mounaimrousselle, C.; Mauss, F. *Proc. Combust. Inst.* **2009**, *32* (1), 753. doi: 10.1016/j.proci.2008.06.115
- (34) Raj, A.; Prada, I. D. C.; Amer, A. A.; Chung, S. H. *Combust. Flame* **2011**, *159* (2), 500.
- (35) Sivaramakrishnan, R.; Tranter, R. S.; Brezinsky, K. *J. Phys. Chem. A* **2006**, *110* (30), 9388. doi: 10.1021/jp060820j
- (36) Detilleux, V.; Vandooren, J. *Proc. Combust. Inst.* **2011**, *33* (1), 217. doi: 10.1016/j.proci.2010.06.151
- (37) Zhang, H. R.; Eddings, E. G.; Sarofim, A. F. *Energy Fuels* **2007**, *21* (2), 677. doi: 10.1021/ef060195h
- (38) Zhang, H. R.; Eddings, E. G.; Sarofim, A. F. *Energy Fuels* **2008**, *22* (2), 945. doi: 10.1021/ef700526n
- (39) Fenimore, C. P.; Jones, G. W. *J. Phys. Chem.* **1967**, *71* (3), 593. doi: 10.1021/j100862a021
- (40) Neoh, K.; Howard, J.; Sarofim, A. *Symposium (International) on Combustion* **1985**, *20* (1), 951.
- (41) Kellerer, H.; Müller, A.; Bauer, H. J.; Wittig, S. *Combust. Sci. Technol.* **1996**, *113* (1), 67. doi: 10.1080/00102209608935488
- (42) Alexiou, A.; Williams, A. *Combust. Flame* **1996**, *104* (1), 51.
- (43) Sakai, Y.; Miyoshi, A.; Koshi, M.; Pitz, W. J. *Proc. Combust. Inst.* **2009**, *32* (1), 411. doi: 10.1016/j.proci.2008.06.154
- (44) Andrae, J. C.; Brinck, T.; Kalghatgi, G. *Combustion and Flame* **2008**, *155* (4), 696. doi: 10.1016/j.combustflame.2008.05.010
- (45) Bakali, A.; Delfau, J. L.; Vovelle, C. *Combust. Sci. Technol.* **1998**, *140* (1-6), 69. doi: 10.1080/00102209808915768
- (46) Frenklach, M.; Yuan, T.; Ramachandra, M. *Energy Fuels* **1988**, *2* (4), 462. doi: 10.1021/ef00010a013
- (47) Hippler, H.; Reihls, C.; Troe, J. *Symposium (International) on Combustion* **1991**, *23* (1), 37.
- (48) Luo, J.; Yao, M. F.; Liu, H. F.; Yang, B. B. *Fuel* **2012**, *97*, 621. doi: 10.1016/j.fuel.2012.02.057

基于不同燃料 PAH 特性改进的适用于多组分燃料的碳烟模型

庞 斌 解茂昭 贾 明* 刘耀东

(大连理工大学能源与动力工程学院, 海洋能源利用与节能教育部重点实验室, 辽宁 大连 116023)

Improved Phenomenological Soot Model for Multicomponent Fuel Based on Variations in PAH Characteristics with Fuel Type

PANG Bin XIE Mao-Zhao JIA Ming* LIU Yao-Dong

(Key Laboratory of Ocean Energy Utilization and Energy Conservation of Ministry of Education,
School of Energy and Power Engineering, Dalian University of Technology, Dalian 116023, Liaoning Province, P.
R. China)

*Corresponding author. Email: jiaming@dlut.edu.cn; Tel: +86-411-84706302.

CHEMKIN output file for TRF-PAH model

Species				
C7H16	O2	CO2	H2O	CO
H2	OH	H2O2	HO2	H
O	CH4	CH3O	CH2O	HCO
CH3	C2H3	C2H4	C2H5	C3H4
C3H5	C3H6	C3H7	C7H15	C7H15O2
O2C7H14OOH	C7KET	C5H11CO	C7H14	C8H18
C8H17	C8H17O2	C8H16OOH	C8KET	O2C8H16OOH
C6H13CO	C8H16	CH2OH	CH3OH	C7H14OOH
C6H5CH2	C6H5CHO	C6H5CO	C6H5O	C4H5
C4H3	C5H5	C5H4O	C5H4OH	C6H5OH
C2H2	CH2CO	HCCO	C5H11	CH2
C2H	C4H4	C3H3	A1	A1-
A2	A2-1	A3	A3-4	A4
A1C2H*	A1C2H	A4-1	C9H8	C9H7
P2	P2-	C6H5CH3		
No. Reactions ($k = AT^n \exp(-E/RT)$)				
	A	n	E	
1. C6H5CH3=C6H5CH2+H	2.09E+15	0.0	87463.4	
2. C6H5CH3=>A1-+CH3	8.66E+15	0.0	97830.4	
3. C6H5CH3+O2=C6H5CH2+HO2	1.50E+14	0.0	41400.0	
4. C6H5CH3+H=A1+CH3	1.20E+13	0.0	5100.0	
5. C6H5CH3+OH=C6H5CH2+H2O	3.00E+12	0.0	1700.0	
6. C6H5CH2+O=C6H5CHO+H	2.11E+14	0.0	0.0	
7. C6H5CH2+O=A1-+CH2O	1.19E+14	0.0	0.0	
8. C6H5CH2+HO2=C6H5CHO+H+OH	1.50E+14	0.0	0.0	
9. C6H5CHO+OH=H2O+C6H5CO	3.44E+09	1.2	-447.0	
10. C6H5CHO+H=H2+C6H5CO	2.28E+10	1.1	3279.0	
11. C6H5CO=A1-+CO	3.00E+12	0.0	34860.0	
12. C6H5O=C5H5+CO	3.76E+54	-12.1	72800.0	
13. C6H5O+H=C6H5OH	2.50E+14	0.0	0.0	
14. C6H5OH+O2=C6H5O+HO2	1.00E+13	0.0	38000.0	
15. C6H5OH+H=C6H5O+H2	1.20E+14	0.0	12400.0	
16. C6H5OH+O=C6H5O+OH	1.30E+13	0.0	2900.0	
17. C6H5OH+OH=C6H5O+H2O	3.00E+06	2.0	-1310.0	
18. C6H5OH+HO2=C6H5O+H2O2	1.00E+12	0.0	1000.0	
19. C5H5+O=C4H5+CO	4.20E+13	-0.2	440.0	
20. C5H5+OH=C5H4OH+H	3.50E+57	-12.2	48350.0	
21. C5H4OH=C5H4O+H	2.10E+13	0.0	54000.0	
22. C5H4O=>C2H2+C2H2+CO	5.70E+32	-6.8	68500.0	
Declared duplicate reaction...				
23. C5H4O=>C2H2+C2H2+CO	6.20E+41	-7.9	98700.0	
Declared duplicate reaction...				

24. $C_4H_5=C_2H_2+C_2H_3$	1.00E+14	0.0	43890.0
25. $A_1+O_2=C_6H_5O+O$	5.60E+11	0.0	6100.0
26. $A_1+OH=A_1+H_2O$	1.63E+08	1.4	1451.0
27. $A_1+O=A_1+OH$	2.00E+13	0.0	14700.0
28. $C_7H_{16}+O_2=C_7H_{15}+HO_2$	1.00E+16	0.0	46000.0
Reverse Arrhenius coefficients:	1.00E+12	0.0	0.0
29. $C_7H_{15}+O_2=C_7H_{15}O_2$	3.00E+12	0.0	0.0
Reverse Arrhenius coefficients:	2.51E+13	0.0	27400.0
30. $C_7H_{15}O_2=C_7H_{14}OOH$	1.51E+11	0.0	19000.0
Reverse Arrhenius coefficients:	1.00E+11	0.0	11000.0
31. $C_7H_{14}OOH+O_2=O_2C_7H_{14}OOH$	6.16E+10	0.0	0.0
Reverse Arrhenius coefficients:	2.51E+13	0.0	27400.0
32. $O_2C_7H_{14}OOH=>C_7KET+OH$	8.91E+10	0.0	17000.0
33. $C_7KET=>C_5H_{11}CO+CH_2O+OH$	3.98E+15	0.0	43000.0
34. $C_5H_{11}CO+O_2=>C_3H_7+C_2H_3+CO+HO_2$	3.16E+13	0.0	10000.0
35. $C_7H_{16}+OH=>C_7H_{15}+H_2O$	5.00E+13	0.0	3000.0
36. $C_7H_{15}+O_2=C_7H_{14}+HO_2$	3.16E+11	0.0	6000.0
Reverse Arrhenius coefficients:	3.16E+11	0.0	19500.0
37. $C_7H_{14}+O_2=>C_3H_6+C_2H_5+CH_2O+HCO$	3.16E+13	0.0	10000.0
38. $C_7H_{16}+HO_2=>C_7H_{15}+H_2O_2$	1.00E+13	0.0	16950.0
39. $C_7H_{15}=>C_3H_6+C_2H_5+C_2H_4$	6.50E+12	0.0	28810.0
40. $C_8H_{18}+O_2=C_8H_{17}+HO_2$	3.00E+16	0.0	46000.0
Reverse Arrhenius coefficients:	1.00E+12	0.0	0.0
41. $C_8H_{17}+O_2=C_8H_{17}O_2$	1.00E+12	0.0	0.0
Reverse Arrhenius coefficients:	2.51E+13	0.0	27400.0
42. $C_8H_{17}O_2=C_8H_{16}OOH$	1.51E+11	0.0	21800.0
Reverse Arrhenius coefficients:	1.00E+11	0.0	11000.0
43. $C_8H_{16}OOH+O_2=O_2C_8H_{16}OOH$	1.16E+11	0.0	0.0
Reverse Arrhenius coefficients:	2.51E+13	0.0	27400.0
44. $O_2C_8H_{16}OOH=>C_8KET+OH$	8.91E+10	0.0	17000.0
45. $C_8KET=>C_6H_{13}CO+CH_2O+OH$	3.98E+15	0.0	43000.0
46. $C_6H_{13}CO+O_2=>C_3H_7+C_3H_5+CO+HO_2$	3.16E+13	0.0	10000.0
47. $C_8H_{18}+OH=>C_8H_{17}+H_2O$	6.00E+14	0.0	3000.0
48. $C_8H_{17}+O_2=C_8H_{16}+HO_2$	4.16E+11	0.0	6000.0
Reverse Arrhenius coefficients:	3.16E+11	0.0	19500.0
49. $C_8H_{16}+O_2=>C_3H_7+C_3H_6+CH_2O+HCO$	3.16E+13	0.0	10000.0
50. $C_8H_{18}+HO_2=>C_8H_{17}+H_2O_2$	1.00E+13	0.0	16950.0
51. $C_8H_{17}=>C_3H_7+C_3H_6+C_2H_4$	4.12E+17	-1.3	29700.0
52. $C_3H_7=C_2H_4+CH_3$	9.60E+13	0.0	30950.0
53. $C_3H_7=C_3H_6+H$	1.25E+14	0.0	36900.0
54. $C_3H_6=C_2H_3+CH_3$	3.15E+15	0.0	85500.0
55. $C_3H_6+CH_3=C_3H_5+CH_4$	9.00E+12	0.0	8480.0
56. $C_3H_5+O_2=C_3H_4+HO_2$	6.00E+11	0.0	10000.0
57. $C_3H_4+OH=C_2H_3+CH_2O$	1.00E+12	0.0	0.0

58. C3H4+OH=C2H4+HCO	1.00E+12	0.0	0.0
59. C2H5+O2=C2H4+HO2	2.00E+10	0.0	-2200.0
60. C2H4+OH=CH2O+CH3	6.00E+13	0.0	960.0
61. C2H4+OH=C2H3+H2O	8.02E+13	0.0	5955.0
62. C2H3+O2=CH2O+HCO	4.00E+12	0.0	-250.0
63. C2H3+HCO=C2H4+CO	6.03E+13	0.0	0.0
64. C3H5=C2H2+CH3	2.40E+48	-9.9	82080.0
Reverse Arrhenius coefficients:	2.61E+46	-9.8	36950.0
65. C2H4(+M)=C2H2+H2(+M)	1.80E+13	0.0	76000.0
Low pressure limit: 0.15000E+16	0.00000E+00	0.55440E+05	
66. C2H3+O2=C2H2+HO2	2.12E-06	6.0	9484.0
Reverse Arrhenius coefficients:	1.11E-07	6.3	17570.0
67. C2H3+H=C2H2+H2	2.00E+13	0.0	2500.0
Reverse Arrhenius coefficients:	1.33E+13	0.0	68080.0
68. C2H2+H(+M)=C2H3(+M)	3.11E+11	0.6	2589.0
Low pressure limit: 0.22540E+41	-0.72690E+01	0.65770E+04	
TROE centering: 0.10000E+01	0.10000E-14	0.67500E+03	0.10000E+16
H2	Enhanced by 2.000E+00		
H2O	Enhanced by 5.000E+00		
CO	Enhanced by 2.000E+00		
CO2	Enhanced by 3.000E+00		
69. C2H2+O2=HCCO+OH	2.00E+08	1.5	30100.0
Reverse Arrhenius coefficients:	2.23E+05	1.5	25400.0
70. C2H2+O=HCCO+H	1.43E+07	2.0	1900.0
Reverse Arrhenius coefficients:	2.02E+05	2.0	13310.0
71. C2H2+OH=CH2CO+H	2.19E-04	4.5	-1000.0
Reverse Arrhenius coefficients:	2.16E-03	4.5	19660.0
72. CH2CO+H=CH3+CO	1.10E+13	0.0	3400.0
Reverse Arrhenius coefficients:	2.40E+12	0.0	40200.0
73. CH2CO+O=HCCO+OH	1.00E+13	0.0	8000.0
Reverse Arrhenius coefficients:	1.43E+10	0.0	-1255.0
74. CH2CO+OH=HCCO+H2O	1.00E+13	0.0	2000.0
Reverse Arrhenius coefficients:	1.41E+11	0.0	9995.0
75. CH2CO+H=HCCO+H2	2.00E+14	0.0	8000.0
Reverse Arrhenius coefficients:	6.52E+11	0.0	840.0
76. HCCO+OH=HCO+HCO	1.00E+13	0.0	0.0
Reverse Arrhenius coefficients:	2.41E+14	0.0	40360.0
77. HCCO+O=H+CO+CO	8.00E+13	0.0	0.0
Reverse Arrhenius coefficients:	0.00E+00	0.0	0.0
78. HCCO+O2=CO2+HCO	2.40E+11	0.0	-854.0
Reverse Arrhenius coefficients:	1.47E+14	0.0	133600.0
79. H+O2=O+OH	3.55E+15	-0.4	16599.0
80. O+H2=H+OH	5.08E+04	2.7	6290.0
81. H2+OH=H2O+H	2.16E+08	1.5	3430.0

82.	O+H2O=OH+OH	2.97E+06	2.0	13400.0
83.	H2+M=H+H+M	4.58E+19	-1.4	104380.0
	H2	Enhanced by 2.500E+00		
	H2O	Enhanced by 1.200E+01		
	CO	Enhanced by 1.900E+00		
	CO2	Enhanced by 3.800E+00		
84.	O+O+M=O2+M	6.16E+15	-0.5	0.0
	H2	Enhanced by 2.500E+00		
	H2O	Enhanced by 1.200E+01		
	CO	Enhanced by 1.900E+00		
	CO2	Enhanced by 3.800E+00		
85.	O+H+M=OH+M	4.71E+18	-1.0	0.0
	H2	Enhanced by 2.500E+00		
	H2O	Enhanced by 1.200E+01		
	CO	Enhanced by 1.900E+00		
	CO2	Enhanced by 3.800E+00		
86.	H+OH+M=H2O+M	3.80E+22	-2.0	0.0
	H2	Enhanced by 2.500E+00		
	H2O	Enhanced by 1.200E+01		
	CO	Enhanced by 1.900E+00		
	CO2	Enhanced by 3.800E+00		
87.	H+O2(+M)=HO2(+M)	1.48E+12	0.6	0.0
	Low pressure limit:	0.63660E+21	-0.17200E+01	0.52480E+03
	TROE centering:	0.80000E+00	0.10000E-29	0.10000E+31
	H2	Enhanced by 2.000E+00		
	H2O	Enhanced by 1.100E+01		
	O2	Enhanced by 7.800E-01		
	CO	Enhanced by 1.900E+00		
	CO2	Enhanced by 3.800E+00		
88.	HO2+H=H2+O2	1.66E+13	0.0	823.0
89.	HO2+H=OH+OH	7.08E+13	0.0	295.0
90.	HO2+O=O2+OH	3.25E+13	0.0	0.0
91.	HO2+OH=H2O+O2	2.89E+13	0.0	-497.0
92.	HO2+HO2=H2O2+O2	4.20E+14	0.0	11982.0
	Declared duplicate reaction...			
93.	HO2+HO2=H2O2+O2	1.30E+11	0.0	-1629.3
	Declared duplicate reaction...			
94.	H2O2(+M)=OH+OH(+M)	2.95E+14	0.0	48430.0
	Low pressure limit:	0.12020E+18	0.00000E+00	0.45500E+05
	TROE centering:	0.50000E+00	0.10000E-29	0.10000E+31
	H2	Enhanced by 2.500E+00		
	H2O	Enhanced by 1.200E+01		
	CO	Enhanced by 1.900E+00		
	CO2	Enhanced by 3.800E+00		

95. $\text{H}_2\text{O}_2 + \text{H} = \text{H}_2\text{O} + \text{OH}$	2.41E+13	0.0	3970.0
96. $\text{H}_2\text{O}_2 + \text{H} = \text{HO}_2 + \text{H}_2$	4.82E+13	0.0	7950.0
97. $\text{H}_2\text{O}_2 + \text{O} = \text{OH} + \text{HO}_2$	9.55E+06	2.0	3970.0
98. $\text{H}_2\text{O}_2 + \text{OH} = \text{HO}_2 + \text{H}_2\text{O}$	1.00E+12	0.0	0.0
Declared duplicate reaction...			
99. $\text{H}_2\text{O}_2 + \text{OH} = \text{HO}_2 + \text{H}_2\text{O}$	5.80E+14	0.0	9557.0
Declared duplicate reaction...			
100. $\text{CO} + \text{O}(+\text{M}) = \text{CO}_2(+\text{M})$	1.80E+10	0.0	2384.0
Low pressure limit: 0.15500E+25 -0.27900E+01 0.41910E+04			
H2	Enhanced by 2.500E+00		
H2O	Enhanced by 1.200E+01		
CO	Enhanced by 1.900E+00		
CO2	Enhanced by 3.800E+00		
101. $\text{CO} + \text{O}_2 = \text{CO}_2 + \text{O}$	2.53E+12	0.0	47700.0
102. $\text{CO} + \text{HO}_2 = \text{CO}_2 + \text{OH}$	3.01E+13	0.0	23000.0
103. $\text{CO} + \text{OH} = \text{CO}_2 + \text{H}$	2.23E+05	1.9	-1158.7
104. $\text{HCO} + \text{M} = \text{H} + \text{CO} + \text{M}$	4.75E+11	0.7	14874.0
H2	Enhanced by 2.500E+00		
H2O	Enhanced by 6.000E+00		
CO	Enhanced by 1.900E+00		
CO2	Enhanced by 3.800E+00		
105. $\text{HCO} + \text{O}_2 = \text{CO} + \text{HO}_2$	7.58E+12	0.0	410.0
106. $\text{HCO} + \text{H} = \text{CO} + \text{H}_2$	7.23E+13	0.0	0.0
107. $\text{HCO} + \text{O} = \text{CO} + \text{OH}$	3.02E+13	0.0	0.0
108. $\text{HCO} + \text{OH} = \text{CO} + \text{H}_2\text{O}$	3.02E+13	0.0	0.0
109. $\text{HCO} + \text{O} = \text{CO}_2 + \text{H}$	3.00E+13	0.0	0.0
110. $\text{HCO} + \text{HO}_2 = \text{CO}_2 + \text{OH} + \text{H}$	3.00E+13	0.0	0.0
111. $\text{HCO} + \text{CH}_3 = \text{CO} + \text{CH}_4$	1.20E+14	0.0	0.0
112. $\text{HCO} + \text{HCO} = \text{H}_2 + \text{CO} + \text{CO}$	3.00E+12	0.0	0.0
113. $\text{HCO} + \text{HCO} = \text{CH}_2\text{O} + \text{CO}$	3.00E+13	0.0	0.0
114. $\text{CH}_2\text{O} + \text{M} = \text{HCO} + \text{H} + \text{M}$	3.30E+39	-6.3	99900.0
H2	Enhanced by 2.500E+00		
H2O	Enhanced by 1.200E+01		
CO	Enhanced by 1.900E+00		
CO2	Enhanced by 3.800E+00		
115. $\text{CH}_2\text{O} + \text{M} = \text{CO} + \text{H}_2 + \text{M}$	3.10E+45	-8.0	97510.0
H2	Enhanced by 2.500E+00		
H2O	Enhanced by 1.200E+01		
CO	Enhanced by 1.900E+00		
CO2	Enhanced by 3.800E+00		
116. $\text{CH}_2\text{O} + \text{H} = \text{HCO} + \text{H}_2$	5.74E+07	1.9	2748.6
117. $\text{CH}_2\text{O} + \text{O} = \text{HCO} + \text{OH}$	1.81E+13	0.0	3080.0
118. $\text{CH}_2\text{O} + \text{OH} = \text{HCO} + \text{H}_2\text{O}$	3.43E+09	1.2	-447.0
119. $\text{CH}_2\text{O} + \text{O}_2 = \text{HCO} + \text{HO}_2$	1.23E+06	3.0	52000.0

120. CH ₂ O+HO ₂ =HCO+H ₂ O ₂	4.11E+04	2.5	10210.0
121. CH ₂ O+CH ₃ =HCO+CH ₄	3.64E-06	5.4	998.0
122. CH ₃ +O=CH ₂ O+H	8.43E+13	0.0	0.0
123. CH ₃ +O ₂ =CH ₃ O+O	1.99E+18	-1.6	29230.0
124. CH ₃ +O ₂ =CH ₂ O+OH	3.74E+11	0.0	14640.0
125. CH ₃ +HO ₂ =CH ₃ O+OH	2.41E+10	0.8	-2325.0
126. CH ₃ +H(+M)=CH ₄ (+M)	1.27E+16	-0.6	383.0
Low pressure limit: 0.24770E+34 -0.47600E+01 0.24400E+04			
TROE centering: 0.78300E+00 0.74000E+02 0.29410E+04 0.69640E+04			
H ₂	Enhanced by 2.000E+00		
H ₂ O	Enhanced by 6.000E+00		
CH ₄	Enhanced by 2.000E+00		
CO	Enhanced by 1.500E+00		
CO ₂	Enhanced by 2.000E+00		
127. CH ₄ +H=CH ₃ +H ₂	5.47E+07	2.0	11210.0
128. CH ₄ +O=CH ₃ +OH	3.15E+12	0.5	10290.0
129. CH ₄ +OH=CH ₃ +H ₂ O	5.72E+06	2.0	2639.0
130. CH ₃ +HO ₂ =CH ₄ +O ₂	3.16E+12	0.0	0.0
131. CH ₄ +HO ₂ =CH ₃ +H ₂ O ₂	1.81E+11	0.0	18580.0
132. CH ₂ OH+M=CH ₂ O+H+M	1.00E+14	0.0	25100.0
133. CH ₂ OH+H=CH ₂ O+H ₂	6.00E+12	0.0	0.0
134. CH ₂ OH+H=CH ₃ +OH	9.64E+13	0.0	0.0
135. CH ₂ OH+O=CH ₂ O+OH	4.20E+13	0.0	0.0
136. CH ₂ OH+OH=CH ₂ O+H ₂ O	2.40E+13	0.0	0.0
137. CH ₂ OH+O ₂ =CH ₂ O+HO ₂	2.41E+14	0.0	5017.0
Declared duplicate reaction...			
138. CH ₂ OH+O ₂ =CH ₂ O+HO ₂	1.51E+15	-1.0	0.0
Declared duplicate reaction...			
139. CH ₂ OH+HO ₂ =CH ₂ O+H ₂ O ₂	1.20E+13	0.0	0.0
140. CH ₂ OH+HCO=CH ₃ OH+CO	1.00E+13	0.0	0.0
141. CH ₂ OH+HCO=CH ₂ O+CH ₂ O	1.50E+13	0.0	0.0
142. 2CH ₂ OH=CH ₃ OH+CH ₂ O	3.00E+12	0.0	0.0
143. CH ₂ OH+CH ₃ O=CH ₃ OH+CH ₂ O	2.40E+13	0.0	0.0
144. CH ₃ O+M=CH ₂ O+H+M	8.30E+17	-1.2	15500.0
145. CH ₃ O+H=CH ₃ +OH	3.20E+13	0.0	0.0
146. CH ₃ O+O=CH ₂ O+OH	6.00E+12	0.0	0.0
147. CH ₃ O+OH=CH ₂ O+H ₂ O	1.80E+13	0.0	0.0
148. CH ₃ O+O ₂ =CH ₂ O+HO ₂	9.03E+13	0.0	11980.0
Declared duplicate reaction...			
149. CH ₃ O+O ₂ =CH ₂ O+HO ₂	2.20E+10	0.0	1748.0
Declared duplicate reaction...			
150. CH ₃ O+HO ₂ =CH ₂ O+H ₂ O ₂	3.00E+11	0.0	0.0
151. CH ₃ O+CO=CH ₃ +CO ₂	1.60E+13	0.0	11800.0
152. CH ₃ O+HCO=CH ₃ OH+CO	9.00E+13	0.0	0.0

153. 2CH3O=CH3OH+CH2O	6.00E+13	0.0	0.0
154. OH+CH3(+M)<=>CH3OH(+M)	2.79E+18	-1.4	1330.0
Low pressure limit:	0.40000E+37	-0.59200E+01	0.31400E+04
TROE centering:	0.41200E+00	0.19500E+03	0.59000E+04
0.63940E+04			
H2	Enhanced by 2.000E+00		
H2O	Enhanced by 6.000E+00		
CH4	Enhanced by 2.000E+00		
CO	Enhanced by 1.500E+00		
CO2	Enhanced by 2.000E+00		
155. H+CH2OH(+M)<=>CH3OH(+M)	1.06E+12	0.5	86.0
Low pressure limit:	0.43600E+32	-0.46500E+01	0.50800E+04
TROE centering:	0.60000E+00	0.10000E+03	0.90000E+05 0.10000E+05
H2	Enhanced by 2.000E+00		
H2O	Enhanced by 6.000E+00		
CH4	Enhanced by 2.000E+00		
CO	Enhanced by 1.500E+00		
CO2	Enhanced by 2.000E+00		
156. H+CH3O(+M)<=>CH3OH(+M)	2.43E+12	0.5	50.0
Low pressure limit:	0.46600E+42	-0.74400E+01	0.14080E+05
TROE centering:	0.70000E+00	0.10000E+03	0.90000E+05 0.10000E+05
H2	Enhanced by 2.000E+00		
H2O	Enhanced by 6.000E+00		
CH4	Enhanced by 2.000E+00		
CO	Enhanced by 1.500E+00		
CO2	Enhanced by 2.000E+00		
157. CH3OH+H=CH2OH+H2	3.20E+13	0.0	6095.0
158. CH3OH+H=CH3O+H2	8.00E+12	0.0	6095.0
159. CH3OH+O=CH2OH+OH	3.88E+05	2.5	3080.0
160. CH3OH+OH=CH3O+H2O	1.00E+06	2.1	496.7
161. CH3OH+OH=CH2OH+H2O	7.10E+06	1.8	-596.0
162. CH3OH+O2=CH2OH+HO2	2.05E+13	0.0	44900.0
163. CH3OH+HCO=CH2OH+CH2O	9.64E+03	2.9	13110.0
164. CH3OH+HO2=CH2OH+H2O2	3.98E+13	0.0	19400.0
165. CH3OH+CH3=CH2OH+CH4	3.19E+01	3.2	7172.0
166. CH3O+CH3OH=CH3OH+CH2OH	3.00E+11	0.0	4060.0
167. C8H18=C5H11+C3H7	2.00E+12	0.0	77990.4
168. C7H16=C7H15+H	3.97E+10	-0.9	103200.0
169. C6H5CH2=C5H5+C2H2	1.00E+06	0.0	34879.4
170. C6H5CH2=C4H4+C3H3	8.00E+12	0.0	83376.1
171. CH2+CH2=C2H2+H2	1.20E+13	0.0	800.0
172. CH2+CH2=C2H2+H+H	1.20E+14	0.0	800.0
173. C2H2+O=CH2+CO	4.05E+05	2.0	1900.0
174. C2H2+O=C2H+OH	4.60E+19	-1.4	28950.0

Reverse Arrhenius coefficients:	3.02E+15	-0.6	-1782.0
175. CH ₂ +C ₂ H ₂ =C ₃ H ₃ +H	2.40E+13	0.0	6620.0
176. C ₂ H ₂ +CH ₃ =C ₃ H ₄ +H	2.72E+18	-2.0	20200.0
177. C ₃ H ₄ +H=C ₃ H ₃ +H ₂	1.15E+08	1.9	7530.0
178. C ₃ H ₃ +OH=C ₂ H ₃ +HCO	2.00E+13	0.0	0.0
179. C ₂ H ₂ +C ₂ H ₃ =C ₄ H ₄ +H	4.90E+16	-1.1	11800.0
180. C ₃ H ₃ +C ₂ H ₂ =C ₅ H ₅	6.35E+10	0.0	9995.2
181. C ₃ H ₃ +O ₂ =CH ₂ CO+HCO	3.00E+10	0.0	2878.0
182. C ₃ H ₃ +C ₃ H ₃ =A1	8.56E+19	-2.5	1692.0
183. C ₃ H ₄ +C ₃ H ₃ =A1+H	4.40E+08	0.0	2000.0
184. A1=A1+H	1.29E+62	-12.5	148085.6
185. A1+H=A1+H ₂	2.50E+14	0.0	16000.0
186. A1+CH ₃ =>A1+CH ₄	4.42E+01	3.9	11463.0
187. A1+C ₃ H ₃ =C ₉ H ₈ +H	6.26E+09	2.6	56500.0
188. A1+O=C ₆ H ₅ O+H	2.20E+13	0.0	4530.0
189. A1+OH=C ₆ H ₅ OH+H	1.30E+13	0.0	10600.0
190. A1+C ₄ H ₄ =A2+H	2.50E+29	-4.4	26400.0
191. 2C ₅ H ₅ =A2+2H	6.10E+10	0.0	4888.3
192. A1+C ₂ H ₂ =A1C ₂ H+H	2.50E+29	-4.4	26400.0
193. A1C ₂ H+H=A1C ₂ H*+H ₂	2.50E+14	0.0	16000.0
194. A1C ₂ H+OH=A1C ₂ H*+H ₂ O	1.60E+08	1.4	1450.0
195. A2-1+C ₄ H ₄ =A3+H	2.50E+26	-4.4	26400.0
196. A1+A1-=P2+H	1.10E+23	-2.9	15890.0
197. P2+H=P2+H ₂	2.50E+14	0.0	16000.0
198. P2+C ₂ H ₂ =A3+H	4.60E+06	2.0	7300.0
199. A1C ₂ H*+A1=A3+H	1.10E+24	-2.9	15890.0
200. A1+A1C ₂ H=A3+H	1.10E+24	-2.9	15890.0
201. A3-4+C ₂ H ₂ =A4+H	1.40E+26	-3.4	17800.0
202. C ₉ H ₈ =C ₉ H ₇ +H	1.73E+68	-15.2	116371.9
203. C ₉ H ₇ +C ₉ H ₇ =>A4+C ₂ H ₂ +H ₂	6.39E+29	-4.0	35205.5
204. C ₉ H ₇ +C ₅ H ₅ =>A3+2H	6.39E+29	-4.0	35205.5
205. A2+H=>A2-1+H ₂	2.20E+07	1.9	9829.5
206. A3+H=>A3-4+H ₂	3.00E+08	1.9	9829.5
207. A4+CH ₃ =>A4-1+CH ₄	2.40E+00	3.9	11771.0